Chapter 5 Results

5.1 Data Collection

Nearly six billion events or 3.9 TBytes of data were recorded during the E94-010 experiment for the interaction $^3\vec{\mathrm{He}}(\vec{e}, e')X$. The event rate was about one thousand events per second. Six initial energies of the electron were used (0.86, 1.7, 2.6, 3.4, 4.3 and 5.1 GeV), and there were 38 spectrometer momentum settings (Sec. 2.3). The kinematic coverage ranged from $0.2 < Q^2 < 1.2$ GeV^2 and $0.5 < W < 2.5$ GeV (Figure 5.1).

The data was read out by the Hall A event analyzer ESPACE [71]. ESPACE used the raw data from the detector ADCs and TDCs along with a database of spectrometer constants to create a focal plane vertex (the plane of the VDCs) for each detected particle trajectory. The vertex and track are then traced back through the spectrometer to obtain kinematic information at the interaction vertex. The output of ESPACE is a series of histograms and ntuples which are used to analyze the data.

A number of cuts were applied to each data set in order to select 'good' electrons [48, 72, 73, 70]. These cuts excluded events originating from the target end windows and events that were reconstructed outside of the known acceptance of the detector. Electron identification was determined using the Čerenkov and shower detectors. Finally, a good track recorded by the VDCs was also required.

The complete data set includes information from elastic scattering up to the deep inelastic regime. Data was collected at momentum settings for both longitudinal and transverse target orientations. The polarization of the electron beam was longitudinal throughout the experiment. The GDH integral, $I(Q^2)$, was determined for 0.15

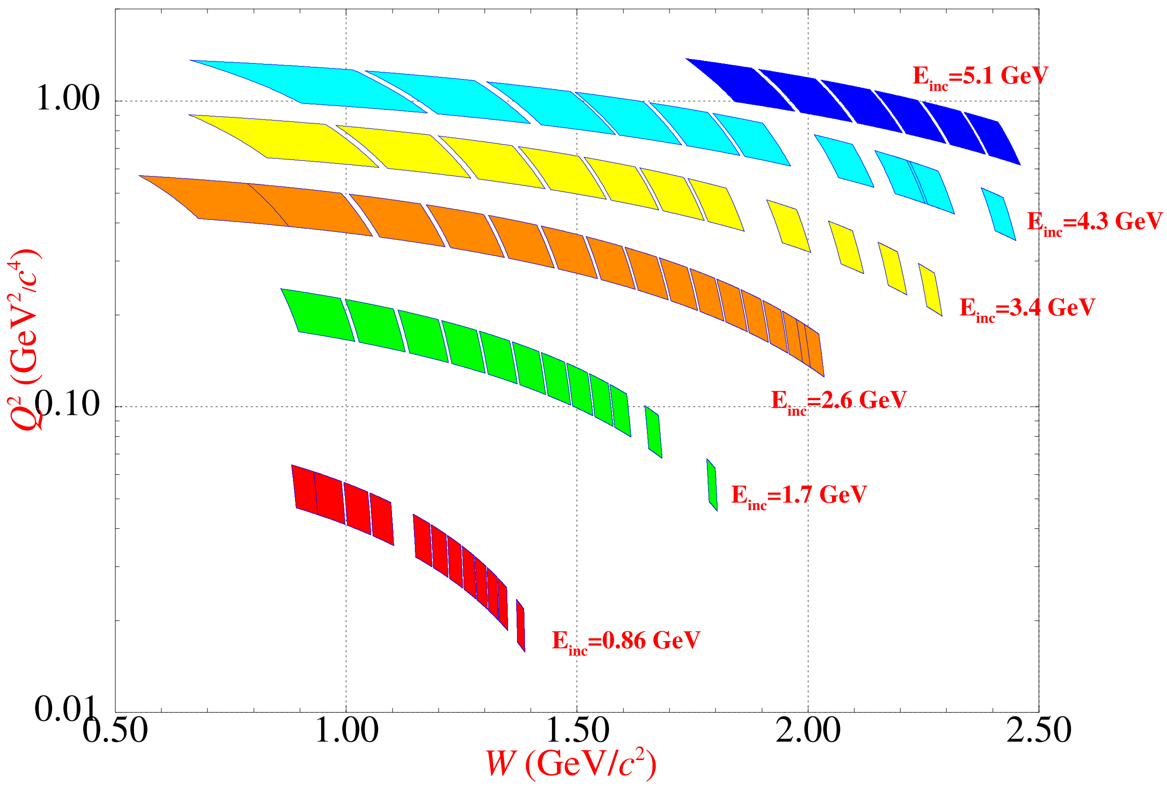

Figure 5.1: Kinematic coverage for E94-010. Each block represents one momentum setting on the spectrometer.

GeV^2 $< Q^2 <$ 1.00 GeV^2.

5.2 Data Analysis

The experiment collected approximately 1800 'runs'. A run is approximately 30 minutes of data collection or 1.8 million events. During and after the data collection, a portion was scanned to evaluate the data quality. Histograms of target reconstruction, acceptance, momentum, deadtime, Čerenkov ADCs, shower ADCs, and scintillator efficiencies were examined for each run.

A few problems were uncovered. The shower detector used in the HRSH spectrometer was found to have a gap between the two sets of lead glass blocks. In addition, the detector was misaligned such that no blocks existed to record the highest momentum electrons. For the present analysis no HRSH shower detector information was used for particle identification. It was also discovered that one of the mirrors in the HRSE Čerenkov detector was misaligned and had, as a result, a very low efficiency. A correction was applied to lower the threshold on what was considered an acceptable ADC value for that mirror. Runs were excluded that demonstrated clear beam instabilities or spectrometer failures.

A number of other issues were studied in detail. The most significant systematic studies are discussed below.

5.2.1 Deadtime

Not every scattered electron is recorded as an event by ESPACE. The computer is limited to about 1 event per 800μs. Since the event rate was around 1000 Hz, most events were recorded. The percentage of events missed is called the 'deadtime' (DT). It is related to the the number of events written to a scalar (S) and the number of events recorded (T):

$$DT = 1 - \frac{T}{S} \tag{5.1}$$

One minus the deadtime is known as the 'livetime' (LT):

Since the computer readout is primarily responsible for the deadtime, it should be independent of the electron beam helicity. However, there are mechanisms that can create false asymmetries in the data. In particular, when there was a period in which the deadtime was fluctuating to large values (50-60%), the overall deadtime experienced when the electron beam had a positive helicity and when it had a negative helicity was not the same. Such periods were observed to occur when data was periodically written to a storage disk. False asymmetries as large as 0.01 occurred on a run-to-run basis.

This effect of a helicity correlated deadtime was observed and studied in the analysis of the $E = 0.86$ GeV and $E = 1.72$ GeV elastic data [70]. Deadtimes were calculated for both positive and negative helicities:

$$DT^{\pm} = 1 - \frac{T^{\pm}}{S^{\pm}}, \tag{5.2}$$

where $T^{\pm}$ and $S^{\pm}$ are the helicity gated number of events written to tape and recorded by a scalar, respectively.

Validity of this method was verified by using data from unpolarized targets: N_2 and ^{12}C. A histogram was created of the measured asymmetry:

$$A = \frac{T^{-} - T^{+}}{T^{-} + T^{+}}. \tag{5.3}$$

During periods of small deadtime fluctuations, the distribution of A had a width of 0.001 and had a gaussian shape. A distribution of A during a period of large fluctuations had a range of ± 0.01. After dividing the rates collected during an unstable period by the helicity correlated livetime ($\frac{T^{\pm}}{LT^{\pm}}$), the distribution of A matched that for a stable period (width of 0.001 and a gaussian shape).

Runs that had large deadtime fluctuations were omitted from the data set. However, the method of calculating separate, helicity correlated, deadtimes was implemented. Generally, the ^{3}He measured asymmetries had values ranging from 0 to -0.02. The amount they changed when the helicity correlated livetime was applied ranged over ± 0.0005.

5.2.2 Optics Study

For each event, four coordinates were recorded: $x_{det}, y_{det}, \theta_{det}$, and ϕ_{det}. The position of the event in the focal plane is described by x_{det} and y_{det}, and the event's trajectory is described by θ_{det} and ϕ_{det}. These observables are used to calculate a set of quantities located at the target [1]: x, y, θ, ϕ, and δ. The two sets of coordinates are connected through a set of tensor relations. Calculation of the tensors required placing targets in the beamline at known positions, recording events, and changing the tensor values until an accurate reconstruction of the target is produced. For a detailed description of this process see [74, 75].

For this experiment, a series of ^{12}C elastic data was taken in order to optimize the tensors for event reconstruction. The carbon target consisted of seven thin carbon foil targets spaced evenly along the beam path (Figure 3.10). The total length covered was 40 cm. Data was collected with and without a sieve slit collimator (Figure 5.2). The sieve slit consisted of 49 holes in a grid pattern. Exact knowledge of the sieve hole positions and the carbon target foils allowed for optimization of the tensors needed for event reconstruction. The results from the optics study are listed in Table 5.1.

Angular resolution (FWHM)		Angle determination accuracy
ϕ	± 2.0 mr	± 0.2 mr
θ	± 6.5 mr	± 0.8 mr
Momentum resolution (FWHM)		
δ at target center	3×10^{-4}	
δ overall	4×10^{-4}	
Transverse position resolution (FWHM)		Transverse position accuracy
y	3.7 mm	± 0.5 mm

Table 5.1: Resolution of the target vertex.

5.2.3 Efficiencies

In order to calculate a cross section, the trigger inefficiency, or percentage of time the trigger did not fire when it should have, needed to be determined. Normally, both planes of scintillators need to fire in order for an event to trigger. By looking

[1] The position of event vertex is given by x and y. The trajectory of the particle from the target is given by ϕ and θ. The event's relative momentum is given by $\delta = \frac{p-p_o}{p_o}$, where p_o is the central momentum of the spectrometer and p is the momentum of the event.

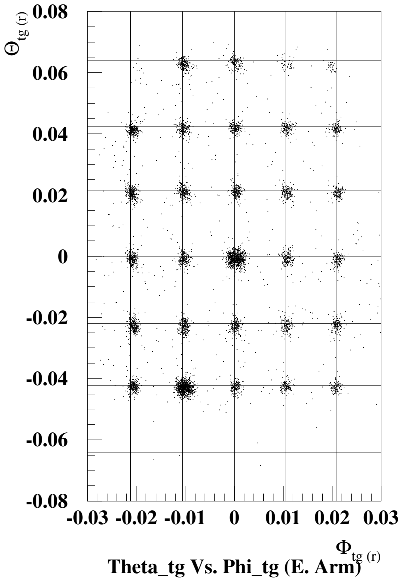

Figure 5.2: Data collected from the carbon target with the sieve slit in. The data represents the location of the events as they enter the spectrometer.

at events that fire only one plane, but otherwise were normal (i.e., a good track from the VDCs and a hit in the shower counter), and comparing those to the number of events that fire both planes, a map of the trigger inefficiency of the focal plane was determined. This map of inefficiency is generated using several runs and is calculated throughout the experiment. The global inefficiency was about 4.3%. The recorded data is corrected for this inefficiency to determine the total absolute event rate.

In addition to the trigger efficiency, efficiencies for the Čerenkov detector, the shower detector, and the VDCs were all determined. Just as in the case of the trigger, each detector was studied by looking at the number of times the detector did not fire when it should have as compared to the number of times it did. For all of the detectors listed above, the efficiencies were found to be >99%.

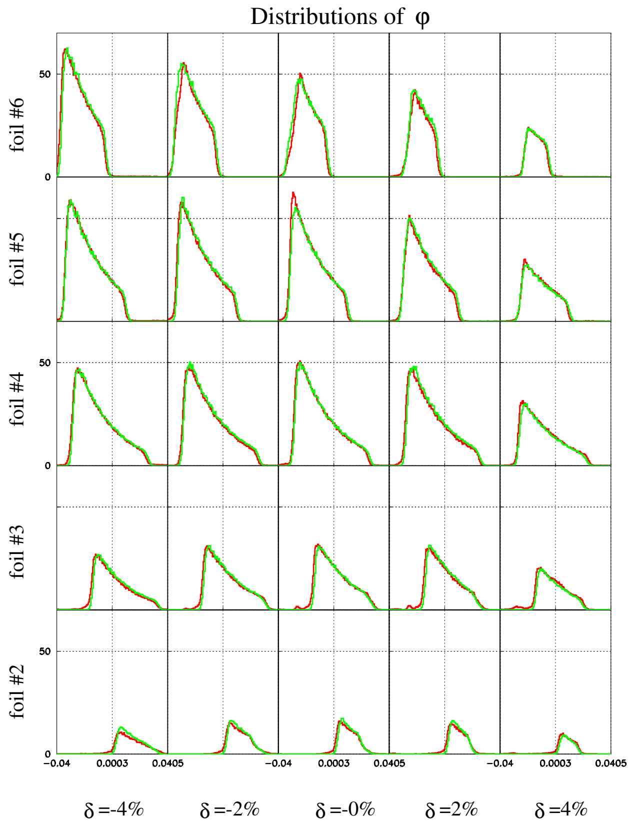

Figure 5.3: A comparison of elastic ^{12}C data (red) and the Monte Carlo (green) distributions for ϕ at the focal plane. Each row is a different carbon foil and each column is a different value of δ: -4%, -2%, 0%, 2%, and 4%.

5.2.4 Monte Carlo

Once the deadtime, spectrometer optics, and efficiencies were understood, a Monte Carlo was developed to understand the angular acceptance and momentum acceptance of the spectrometers [76]. The results of the Monte Carlo were checked against actual ^{12}C elastic data. By folding in the detector efficiencies, the deadtime, and the physics of ^{12}C elastic cross section, the Monte Carlo was able to predict a cross section to within $\pm 4\%$ of the measured results (Figure 5.3). This accuracy is in line with, or slightly better than, previous experiments using the Hall A spectrometers [49].

In addition to the ^{12}C elastic data, the elastic data from ^{3}He was compared to a prediction made by the Monte Carlo. Both the ^{3}He cross section and asymmetry were checked. The cross section agrees within error bars and the asymmetry also shows good agreement when data from both arms are combined (Figures 5.4 and 5.5).

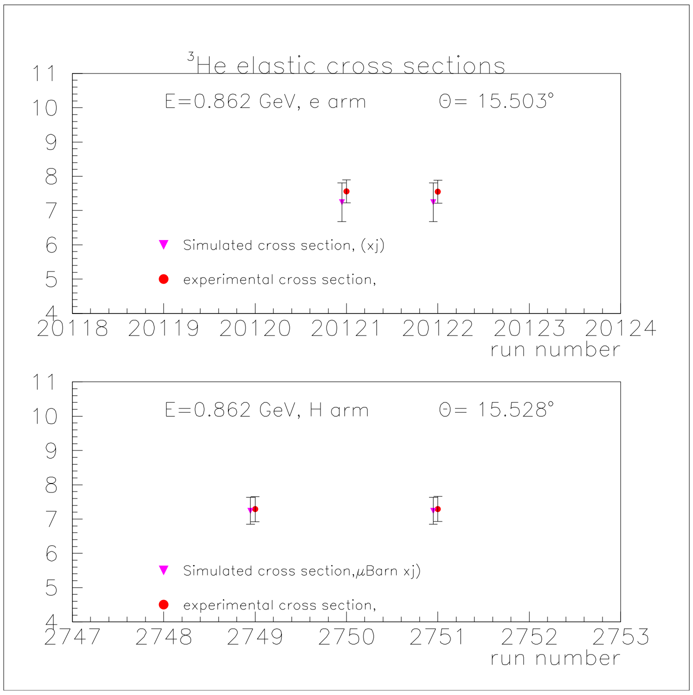

Figure 5.4: Comparison of the $E = 0.86$ GeV elastic data cross section for ^{3}He and the Monte Carlo prediction for two runs. The top plot shows the results from the HRSE spectrometer and the bottom is from the HRSH spectrometer. The vertical scale is in μbarns.

5.2.5 Pion Rejection

As discussed in Sections 2.3.3 and 2.3.4, the Čerenkov and shower detectors were used together to identify and reject pions. The Čerenkov detector, in principal, can reject all pions; however, occasionally a pion will knock off an electron which in turn is detected by the Čerenkov and gives a false identification. The shower detector has the ability to reject pions by measuring the ratio of the deposited energy and

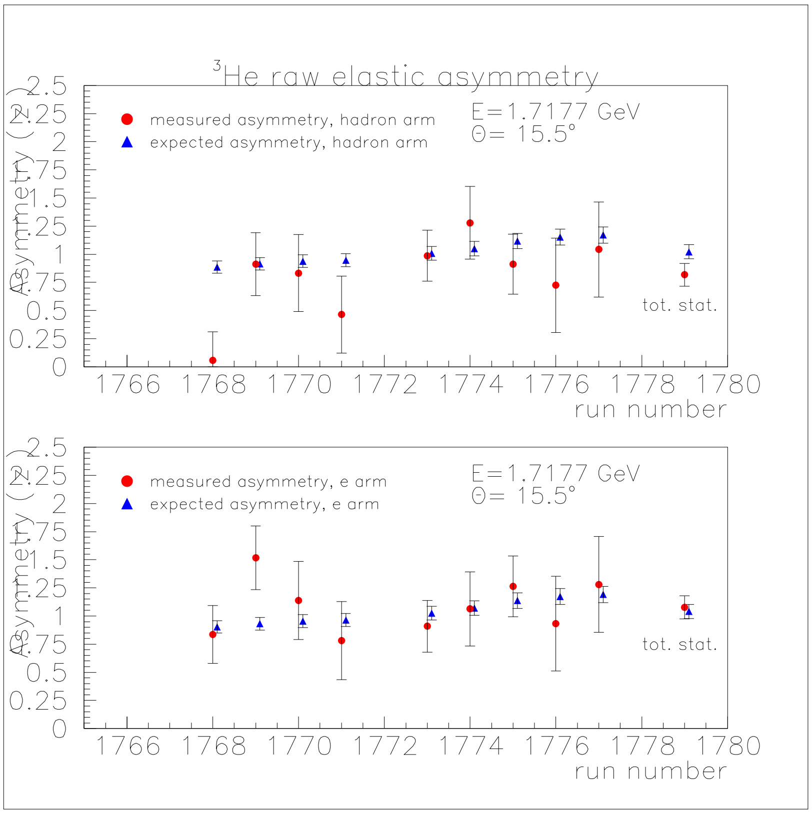

Figure 5.5: Comparison of the $E = 1.72$ GeV elastic data cross section for ^{3}He and the Monte Carlo prediction for two runs. The top plot shows the results from the HRSH spectrometer and the bottom is from the HRSE spectrometer. The vertical scale is in μbarns.

the momentum: E/p (Figure 5.6). The amount of pion contamination is determined by fitting the pion and electron peaks from the shower detector. By comparing results with and without a Čerenkov cut and calculating the amount of pion tail underneath the electron peak, it was found that the ratio of pions to electrons (π/e^-) was negligible: $\approx 10^{-4}$ [72].

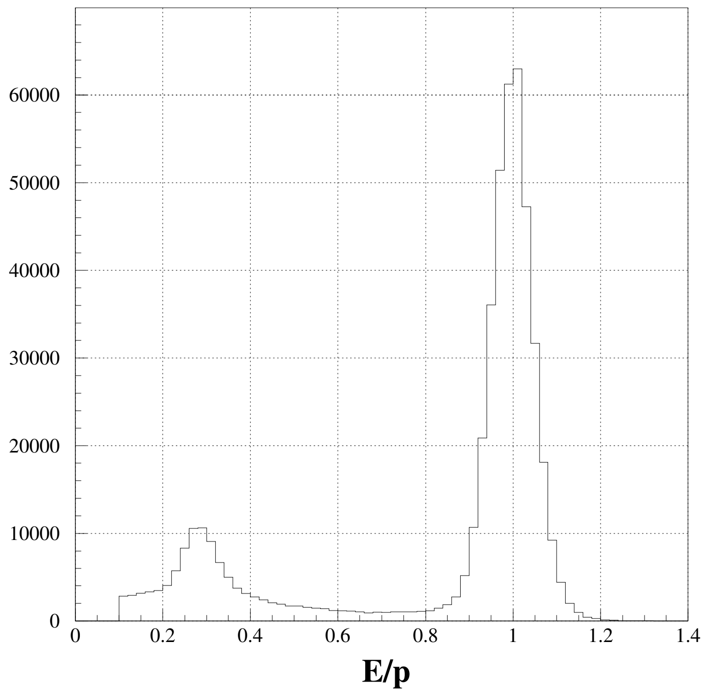

Figure 5.6: The E/p histogram for $E = 3.4$ GeV and $p_o = 2.199$ GeV. A cut on pions can be made by rejecting events with E/p<0.8.

5.2.6 Radiative Corrections

Corrections due to radiative effects (external and internal) were included in the analysis. External radiation involves the loss of electron energy as it passes through matter: external bremsstrahlung. For the E94-010 target, the external corrections included the glass windows and walls of the target and the ^{3}He itself. The effect of the external radiation is to cause a lower interaction energy at the event vertex and a lower perceived scattered energy. Corrections to the data for this type of radiation were done using the technique in [77].

Internal radiation includes emission of a real or virtual photon during the interaction between the electron and the target nuclei. Figure 5.7 shows six possible interactions. Diagrams **a** and **b** represent the emission of a real photon before or after the interaction. Diagrams **c** and **d** represent the emission and re-absorption of a virtual photon by the incident or scattered electron. Diagram **e** represents exchange of a virtual photon between the incident and scattered electron. Diagram **f** represents the renormalization of the virtual photon due to vacuum polarization. Corrections for these types of radiative processes were done using a modified version of the program POLRAD [78, 79].

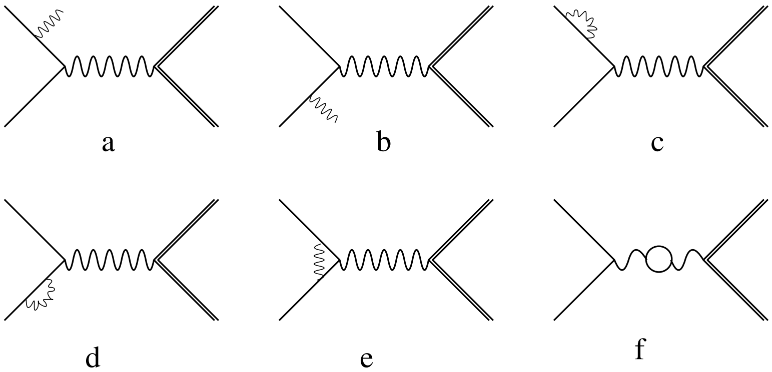

Figure 5.7: Six possible internal radiative processes.

Application of external and internal radiative corrections requires knowledge of the polarized and unpolarized cross sections over a wide kinematic range. These quantities have not been measured in the region of our data. Nuclear models [2] had to be used in order to perform the radiative corrections. The radiative corrections changed the shape of the cross sections dramatically (Figure 5.8), especially for the lower ν bins.

At present, there is no estimation of the uncertainty on the corrections for each ν bin. It is believed that the corrections for higher incident electron energies will later be understood due to further studies from data at lower energies. The corrections to the $E = 0.86$ GeV data are the most suspect because they rely upon models of the ^{3}He polarized cross sections at lower energies. This will in turn affect the corrections to the $E = 1.72$ GeV, which will influence the $E = 2.59$ GeV corrections and so on.

Overall, the radiative corrections dominate the lower incident electron cross sections. For the higher energy cross sections, corrections are as high as 50%. The corrections do not have as great an effect on the asymmetries. Typically, $A_{||}$ and $A_{\perp}$ were affected between 5 and 20% of their values.

5.3 Measured Quantities

For each momentum setting, a differential cross section was measured for each spin configuration of beam and target ($\uparrow\uparrow, \downarrow\uparrow, \uparrow\leftarrow$, and $\downarrow\leftarrow$):

$$\frac{d^2\sigma(\nu, Q^2)}{dEd\Omega} = \frac{N_{goode^-}}{N_e N_t \Delta E \Delta\Omega \varepsilon LT} \times RADCOR \tag{5.4}$$

where N_{goode^-} is the number of 'good' electrons recorded, N_e is the number of incident electrons, N_t is the target thickness in nuclei per unit area, ΔE is the energy width of the spectrometer, $\Delta\Omega$ is the solid angle of the spectrometer, ε represents the total efficiency (namely the multiplication of trigger, tracking, Čerenkov, and shower efficiencies), LT is the computer live-time, and $RADCOR$ is a radiative correction.

The recorded data was used to form two asymmetries:

$$A_{||}(\nu, Q^2) = \frac{1}{P_{beam} P_{target} f} \frac{\frac{N^{\downarrow\uparrow}_{goode^-}}{N_e^{\downarrow} LT^-} - \frac{N^{\uparrow\uparrow}_{goode^-}}{N_e^{\uparrow} LT^+}}{\frac{N^{\downarrow\uparrow}_{goode^-}}{N_e^{\downarrow} LT^-} + \frac{N^{\uparrow\uparrow}_{goode^-}}{N_e^{\uparrow} LT^+}} \tag{5.5}$$

and

$$A_{\perp}(\nu, Q^2) = \frac{1}{P_{beam} P_{target} f} \frac{\frac{N^{\downarrow\leftarrow}_{goode^-}}{N_e^{\downarrow} LT^-} - \frac{N^{\uparrow\leftarrow}_{goode^-}}{N_e^{\uparrow} LT^+}}{\frac{N^{\downarrow\leftarrow}_{goode^-}}{N_e^{\downarrow} LT^-} + \frac{N^{\uparrow\leftarrow}_{goode^-}}{N_e^{\uparrow} LT^+}}, \tag{5.6}$$

where P_{beam} is the polarization of the incident electrons, P_{target} is the polarization of the target, $N^{\uparrow\uparrow(\uparrow\downarrow)}$ is the number of events recorded when the beam and target polarizations are aligned (anti-aligned), $N^{\uparrow\leftarrow(\downarrow\leftarrow)}$ is the number of events recorded when the beam and target polarizations are perpendicular, $N_e^{\uparrow(\downarrow)}$ is the number of incident electrons with positive (negative) helicity, and $LT^{+(-)}$ is the livetime when the initial electron helicity is positive (negative). The dilution factor, f, is the percentage of recorded events originating from the ^{3}He nuclei.

The largest contribution to the dilution comes from the presence of N_2 gas located in the target chamber. For values of ν above the elastic peak,

$$f \approx 1 - \frac{\#\text{ of N}_2\text{ nuclei}}{\#\text{ of }^3\text{He nuclei}} \approx 0.94. \tag{5.7}$$

For values of ν in the region of the ^{3}He elastic peak, the N_2 elastic cross section influences the amount of dilution. Using N_2 elastic data taken using the reference target, it was found [70] that $f \approx 0.99$ for the E=0.86 GeV elastic peak, and $f \approx 0.91$ for the E=1.72 GeV elastic peak.

The results with P_{beam} = 70% and P_{target} = 30% are shown in Figures 5.9 and 5.10.

For both $A_{||}$ and $A_{\perp}$ there is significant dynamic behavior. The asymmetries move from positive to negative values as the scattering moves from one regime to the next. The data for $A_{||}$ (E=3.4 GeV) illustrates this point. For $\nu \approx$ 400 MeV, the quasi-elastic peak is positive. The asymmetry then changes to a large negative value for the Δ resonance at $\nu \approx$650 MeV. It then returns to nearly zero before becoming large and negative again for the higher resonances.

Some general characteristics are noteworthy. For $A_{||}$, the Δ resonance, located at 250 to 750 MeV depending on the energy, is large for all incident energies. It is negative and has a magnitude of ~0.02 over the entire range of incident energies. The quasi-elastic peak for $A_{\perp}$ is negative with magnitude of ~0.02 over the entire range of incident energies. Outside of the quasi-elastic peak for $A_{\perp}$, the asymmetries tend towards zero for increasing beam energy.

The measured quantities in Eq. 5.4 are combined to form relations to the spin structure functions, G_1 and G_2:

$$\frac{1}{P_{beam}P_{target}}\frac{d\sigma}{dE'd\Omega}(\downarrow\uparrow - \uparrow\uparrow) = \frac{4\alpha^2}{M^3Q^2}\frac{E'}{E}[MG_1(E+E'\cos\theta) - Q^2G_2] \tag{5.8}$$

and

$$\frac{1}{P_{beam}P_{target}}\frac{d\sigma}{dE'd\Omega}(\downarrow\leftarrow - \uparrow\leftarrow) = \frac{4\alpha^2}{M^3Q^2}\frac{E'^2}{E}\sin\theta[MG_1 + 2EG_2]. \tag{5.9}$$

These equations are used to solve for G_1 and G_2 (Figures 5.11). There is some noteworthy behavior displayed by the evolution of g_1 and g_2. Large changes were measured from one incident energy to the next for g_1. The value of g_1 goes from about -0.1 to -0.6 when the incident energy is increased from 2.6 to 3.4 GeV. Interestingly, over much of the range shown $g_2 \simeq -g_1$. This is in line with a prediction for the twist-2 contribution to g_2 by Wadzura and Wilcek [80]:

$$g_2^{WW}(x,Q^2) = -g_1(x,Q^2) + \int_x^1 \frac{dx'}{x'}g_1(x',Q^2). \tag{5.10}$$

In regions were ν is small and x fairly high, the contribution of the integral to g_2^{WW} is small, and $g_2 \sim -g_1$.

Comparison of $g_1^{^3He}(Q^2)$ measured by this experiment and that measured by SLAC experiment E154 [3] show good agreement even though the E94-010 data is at a lower Q^2 value (Figure 5.12).

The values for $G_1(\nu,Q^2)$ and $G_2(\nu,Q^2)$ were used to calculate the value of $\sigma_{TT}(\nu,Q^2)$:

$$\sigma_{TT}(\nu,Q^2) = (\sigma_{1/2} - \sigma_{3/2}) = \frac{8\pi^2\alpha}{M^3\left(\nu - \frac{Q^2}{2M}\right)}(M\nu G_1 - Q^2G_2). \tag{5.11}$$

The results for σ_{TT} are shown in Figure 5.13. The Δ and quasi-elastic peaks are now clearly seen. Both peaks have large values and have opposite signs. One challenge from this data is to disentangle the quasi-elastic and Δ peaks, which still overlap. This spillage can most clearly be seen in the E = 2.6 GeV data set. There is a sharp zero crossing at ν =375 MeV. Understanding the contamination is important for calculating the GDH neutron integral.

The uncertainties on $A_{||}$, $A_{\perp}$, and σ_{TT} are primarily dominated by systematic uncertainties. There is a 5% uncertainty due to beam and target polarizations. There is an additional uncertainty on σ_{TT} from the acceptance: ~4%. The spectrometer angle adds an uncertainty of ~1%. The target spin angle adds an uncertainty of ~1% for $A_{||}$ and σ_{TT} and ~5% for $A_{\perp}$. Uncertainties due to the beam energy, deadtime, and dilution are small and have been neglected. Uncertainties on the spectrometer efficiency are currently estimated to be a few percent. Overall there is currently believed to be about a 10% uncertainty from all parameters together, other than the radiative corrections, in both asymmetries and cross section measurements [81].

5.4 The GDH Integral for ^{3}He and the Neutron

Calculation of the GDH integral, $I(Q^2)$, for Q^2 values of 0.03, 0.17, 0.39, 0.66, and 1.04 GeV, was performed by integrating σ_{TT} for each initial energy:

$$I_{GDH}^{He}(\bar{Q^2}) = \sum_{i=\nu_1}^{\nu_f} \frac{\sigma_{TT}(E,\nu_i)}{\nu_i}(\nu_{i+1} - \nu_i), \tag{5.12}$$

where $\bar{Q^2}$ is the Q^2 value at the Δ resonance, ν_i is the value of ν at the zero crossing between the quasi-elastic peak and Δ resonance, and ν_f is the highest value of ν for an incident energy E. This method provides only an approximation to the actual GDH integral for the neutron after extraction, since it integrates primarily over the Δ resonance which is expected to be the dominate contribution. It, however, does a poor job of including contributions from the higher energy resonances especially for the $E = 0.862$ GeV and $E = 1.72$ GeV cases. The integration is carried over constant E, not constant Q^2, as needed to represent properly the integral.

In order to extract neutron results using ^{3}He, the relationship between neutron and

^{3}He polarizations needs to be taken into account. To first order, the ^{3}He wavefunction of Friar *et al.* [21] can be used. From groundstate ^{3}He wavefunction calculations, they showed that the protons within ^{3}He are about 3% polarized in the opposite direction compared to the ^{3}He polarization. The neutron is about 87% polarized in the direction of the ^{3}He polarization. More recently, it was suggested by C. Ciofi degli Atti and S. Scopetta [2] to extract the extended GDH integral using the following relation:

$$\tilde{I}^{He}(Q^2) = 2p_p I^p(Q^2) + p_n I^n(Q^2), \tag{5.13}$$

where I^x is the GDH integral at a particular Q^2 and $p_{p(n)}$ is the effective polarization produced by the S' and D waves in the ground state of ^{3}He. They point out that extraction of $G_1^n(\nu, Q^2)$ using their method works in the deep inelastic region but is limited in the resonance region (the region of interest). However, extraction of a neutron GDH integral from ^{3}He is possible when the appropriate effective polarizations are used. For the purpose of an $I^n(Q^2)$ extraction from the calculated integral of Eq. 5.12, the effective polarizations p_p and p_n are set to 0 and 0.87 respectively. This extraction is shown in Figure 5.14 and listed in Table 5.2. The simple extraction does not follow a proposed evolution of the GDH integral as proposed by Burkert and Li [1], nor does the evolution towards -232.8μb at $Q^2 = 0$ appear likely. A number of effects that could alter the extrapolated values have yet to be fully understood and taken into account.

When the integration includes the quasi-elastic peak, an approximation of the GDH integral for ^{3}He is made. This is also shown in Figure 5.14. The evolution of this curve towards a point at $Q^2 = 0$ appears to be large and positive. This is in sharp contrast to the value of -496μb as predicted by the GDH sum rule.

$\bar{Q}^2$ [GeV]	$I^n_{GDH}(Q^2)$ [μb]
0.03	-62
0.17	-112
0.39	-51
0.66	-29
1.04	-14

Table 5.2: Calculated values of $I^n_{GDH}(\bar{Q}^2)$.

5.5 Interpretation

There are a number of issues yet to be investigated before the simple approximation of the GDH integral for the neutron can be believed. The integration performed using Eq. 5.12 was constant in energy, not constant in Q^2 as is necessary for proper representation of the GDH integral. However, this assumption should not change the results significantly, since most of the weight of the integral lies over the Δ resonance which is mainly at constant Q^2 (0.182 to 0.153 GeV in one case).

Another possible cause for the disagreement between the results using the simple approximation of the GDH integral for the neutron and the calculation done by Burkert and Li could be the existence of quasi-elastic events in the region of integration. The height of the quasi-elastic peak is positive and a factor of four larger compared to the Δ peak for the lower energies (Figure 5.13). These quasi-elastic events could spill into the more heavily weighted low ν bins.

For the two lowest energies, those corresponding to $I^n(\bar{Q}^2{=}0.03\text{ GeV})$ and $I^n(\bar{Q}^2 = 0.17\text{ GeV})$, there is good separation of the quasi-elastic and Δ peaks. Yet, it is these points that disagree the most from prediction.

The cross sections for the other three incident energies do not show a clear separation between peaks. The effect on $I^n(\bar{Q}^2)$ from the quasi-elastic contamination should be small because of the relatively small size of the quasi-elastic peak. The values for $I^n(\bar{Q}^2)$ corresponding to these energies seem in line with the prediction.

Contribution from unmeasured resonances could also move the results. The data for $\sigma_{TT}(E = 0.86 \text{ GeV})$ does not extend high enough in ν to include resonances other than the Δ resonance. These higher energy resonances will increase the value of $I^n(\bar{Q} = 0.03 \text{ GeV})$. Also, further extension in ν for the $\sigma_{TT}(E{=}3.4$ and 4.2 GeV) data sets will increase $I^n(\bar{Q} = 0.66 \text{ GeV})$ and $I^n(\bar{Q} = 1.0 \text{ GeV})$.

Some of these issues can be resolved by studying the radiative corrections to the quasi-elastic peak. With further study the 1.72 GeV data should be corrected. The 0.86 GeV data will probably not be corrected sufficiently to understand the evolution of the cross section because of the lack of lower energy data.

Lastly, there is another possibility as to the apparent discrepancy of the GDH sum rule and the evolution of the GDH integral towards a value at $Q^2{=}0$; the GDH sum rule could itself be incorrect. Of the underlying assumptions made in the derivation of the sum rule, the no subtraction dispersion relation is the most suspect. The no subtraction assumption implies that the value of the Compton scattering amplitude (Eq. 1.66) $f_2(\nu) \to 0$ as $\nu \to \infty$. If it is shown that a subtraction is necessary, it could indicate, among others things [82], that the constituent quarks have an anomalous magnetic moment or, in other words, internal structure. Such conjectures from the results of this experiment would be reckless, but it is interesting and humorous to consider.

Less in question is the GDH integral for ^{3}He. Here the integral is expected to evolve towards larger and larger positive values as $Q^2 \to 0$. Then, suddenly, it is expected to drop towards the real photon point of -496 μb. This is perhaps not as surprising as it seems. The GDH sum rule is a prediction for a real photon. The cross section for a real photon has no elastic or quasi-elastic interactions. Just how the quasi-elastic peak makes the transition from a large positive value, for virtual photons, to zero, for real photons, requires data with real photon beams. More data is required to observe this exciting behavior.

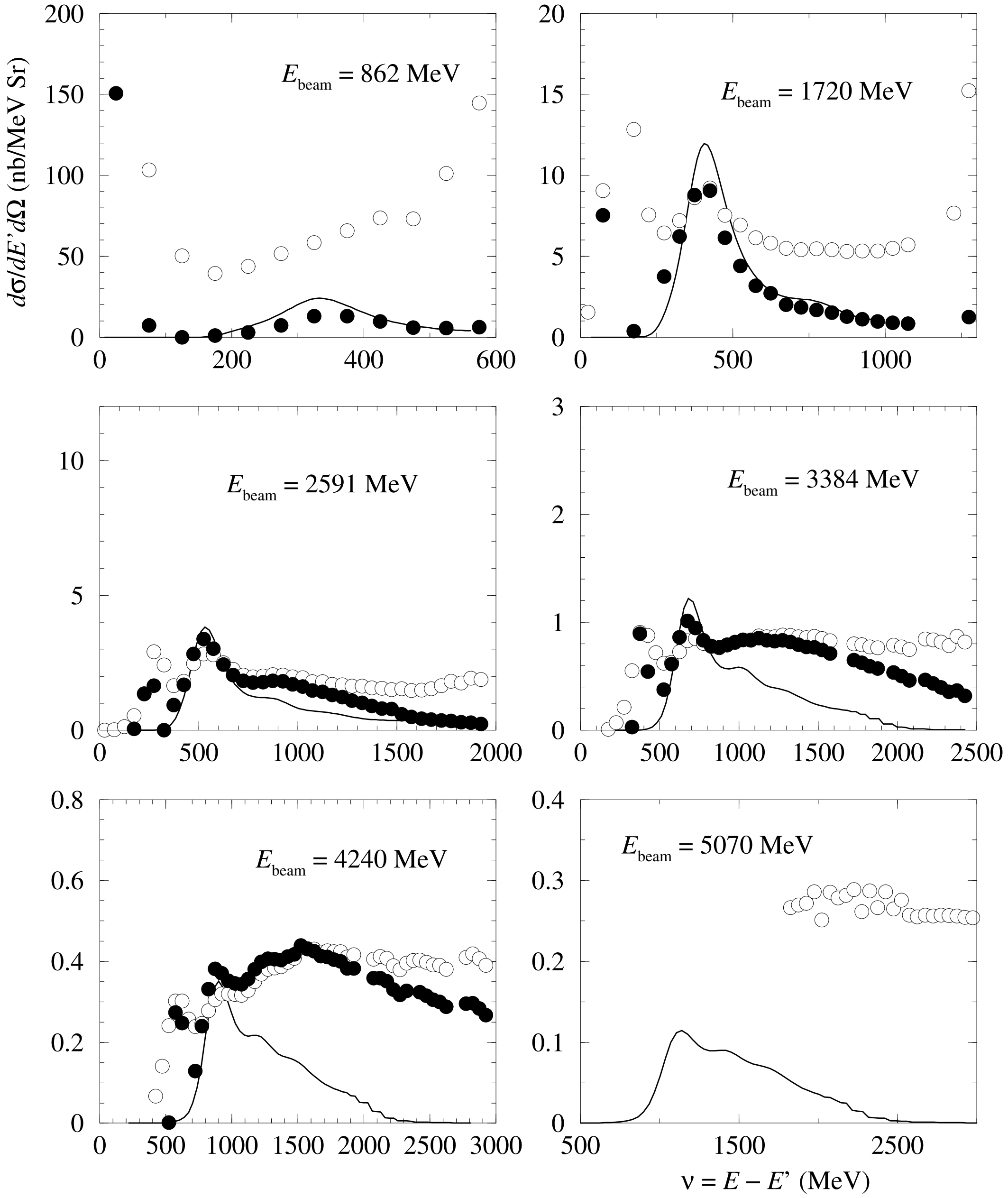

Figure 5.8: The ^{3}He cross section. The open circle points correspond to data without radiative corrections. The solid circle points are after radiative corrections are applied. The solid line is a calculation performed by Scopetta [2].

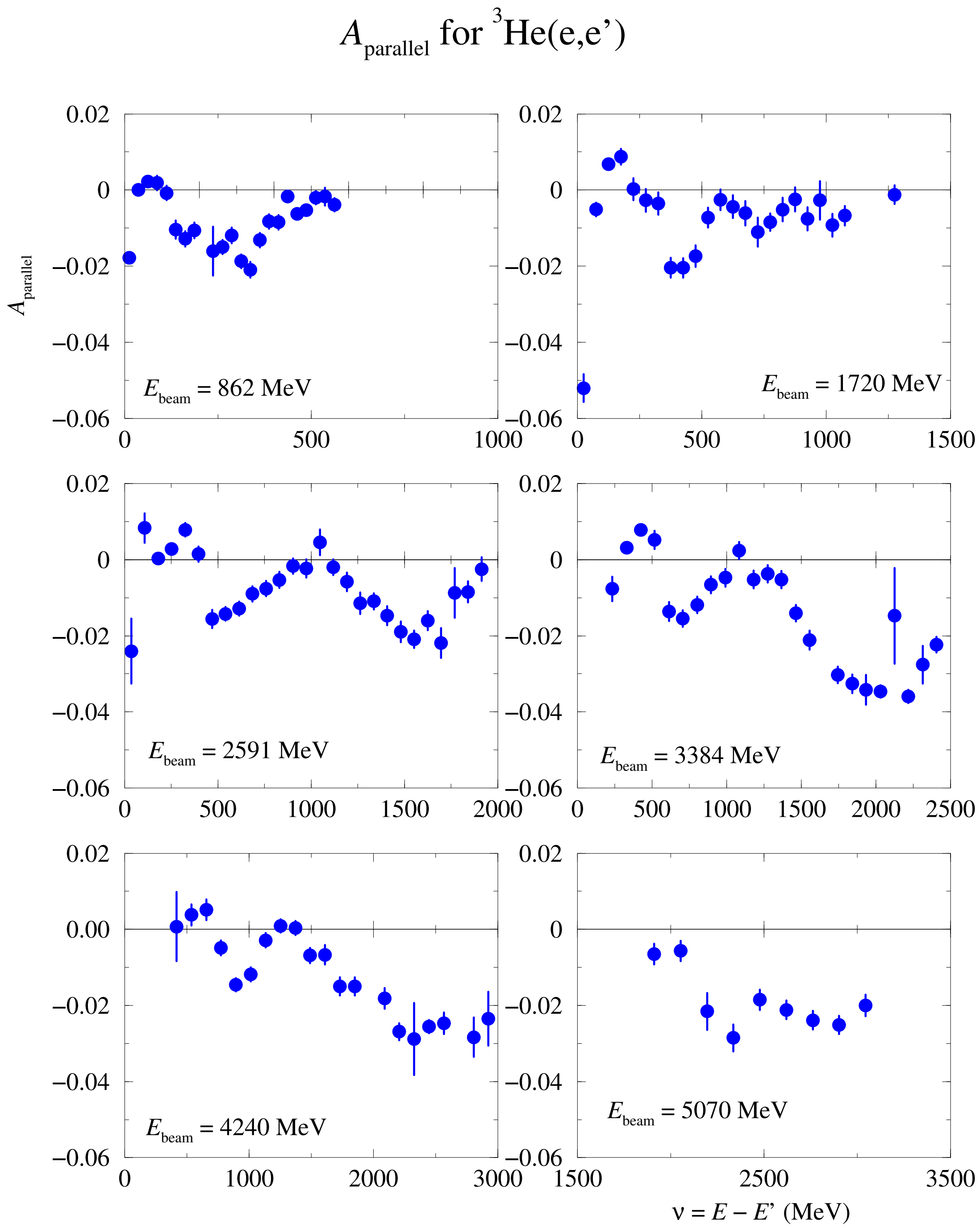

Figure 5.9: $A_{||}$ for the six initial beam energies. Error bars shown are statistical only.

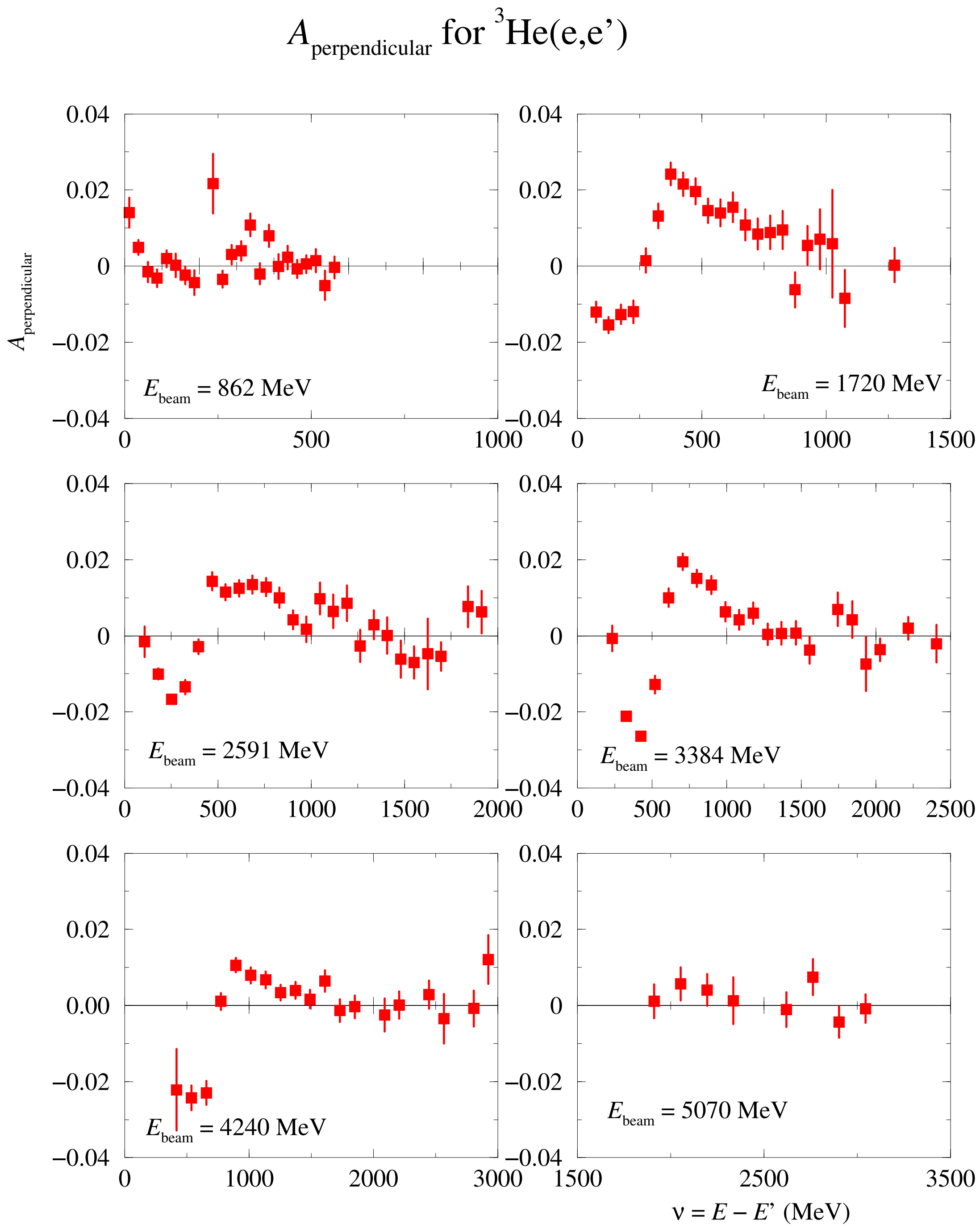

Figure 5.10: $A_\perp$ for the six initial beam energies. Error bars shown are statistical only.

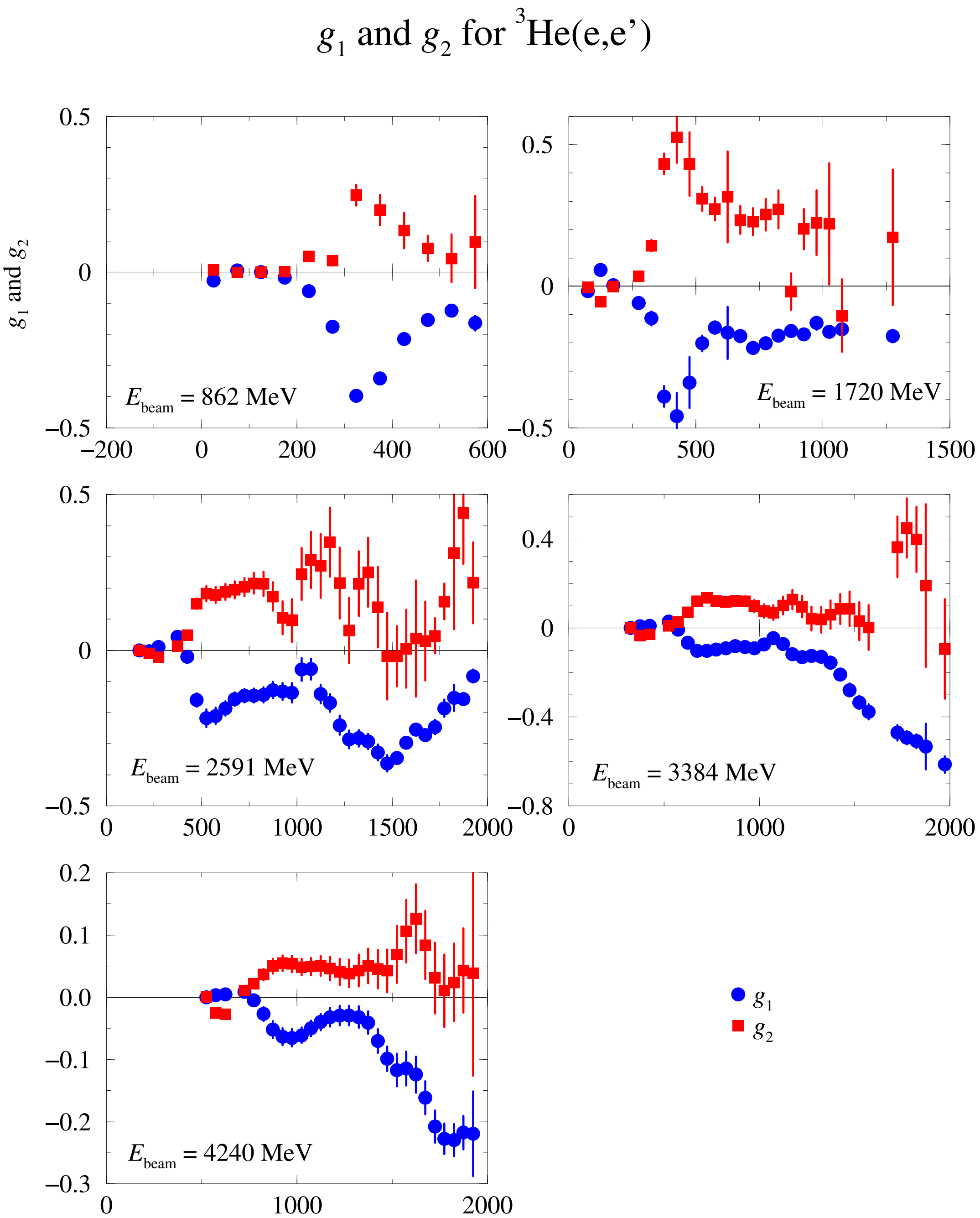

Figure 5.11: Results for the spin dependent structure function $g_1^{^3He}(\nu, Q^2) = \frac{\nu}{M} G_1$ and $g_2^{^3He}(\nu, Q^2) = \frac{\nu^2}{M^2} G_2$. Error bars are statistical only.

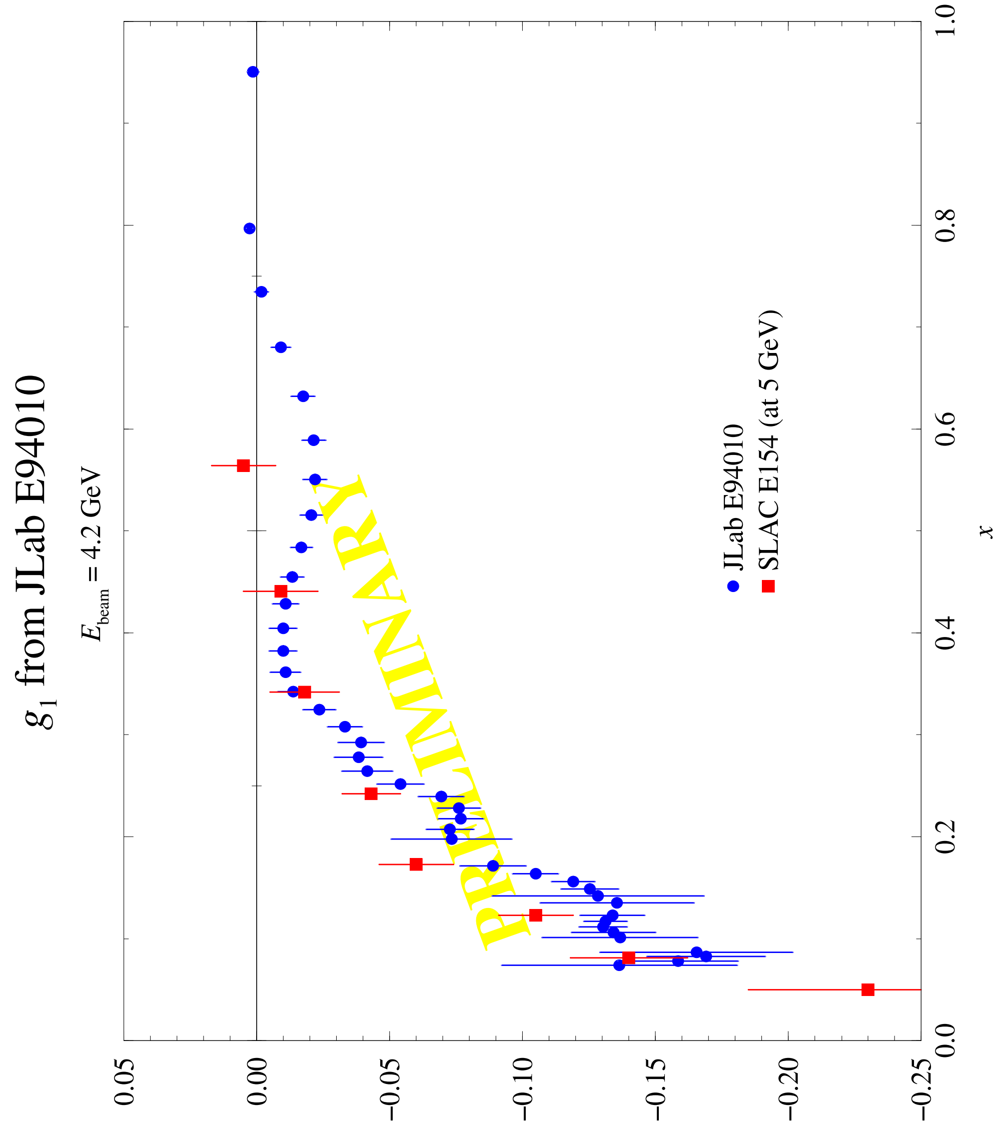

Figure 5.12: Comparison between $g_1^{He}(x) = \frac{\nu}{M} G_1^{He}$ as measured by this experiment and SLAC E154 [3] in the deep inelastic region.

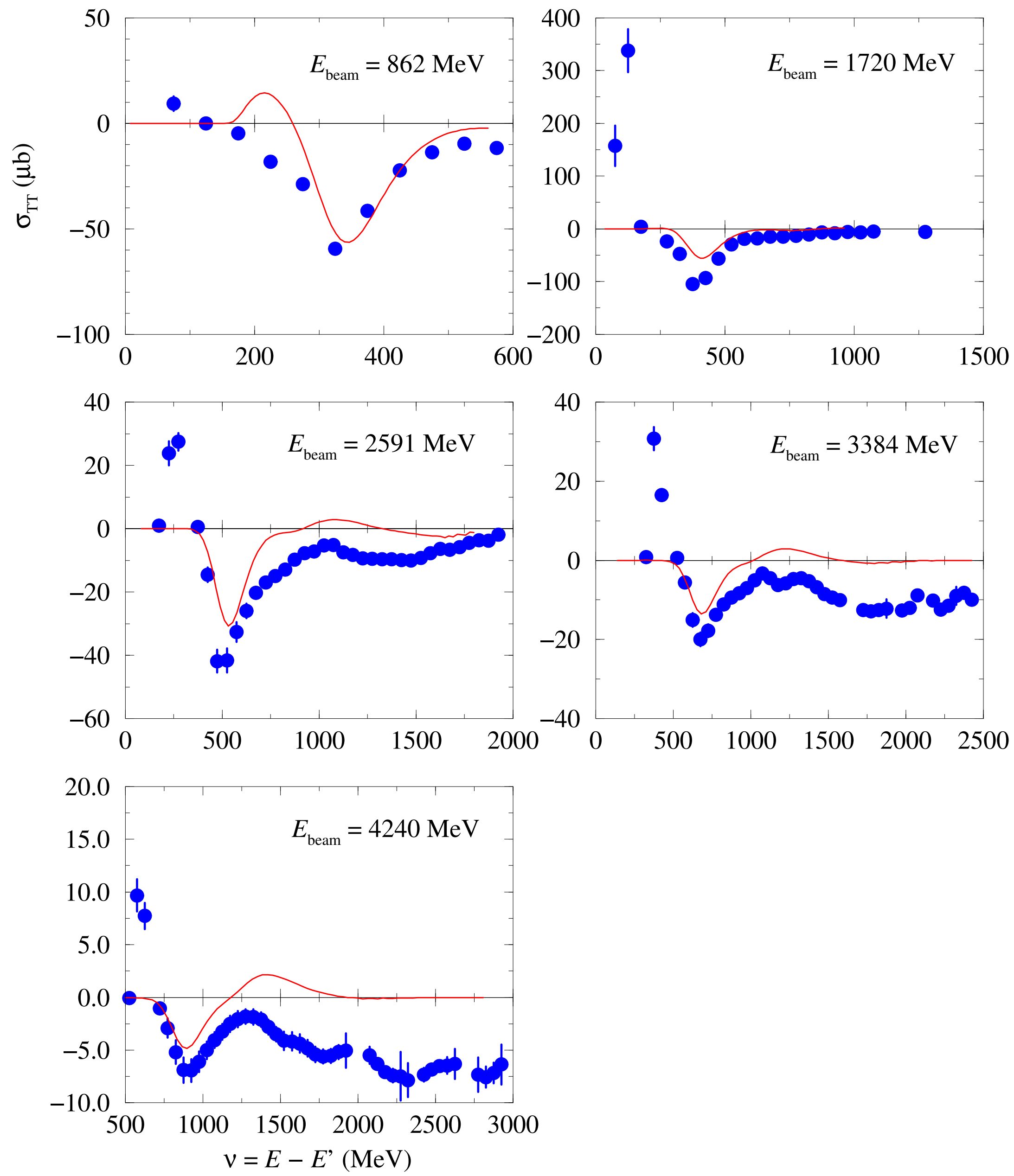

Figure 5.13: σ_{TT} plotted as a function of ν for five of the initial beam energies. Error bars shown are statistical only. The solid line is a calculation for the Δ resonance performed by Scopetta [2].

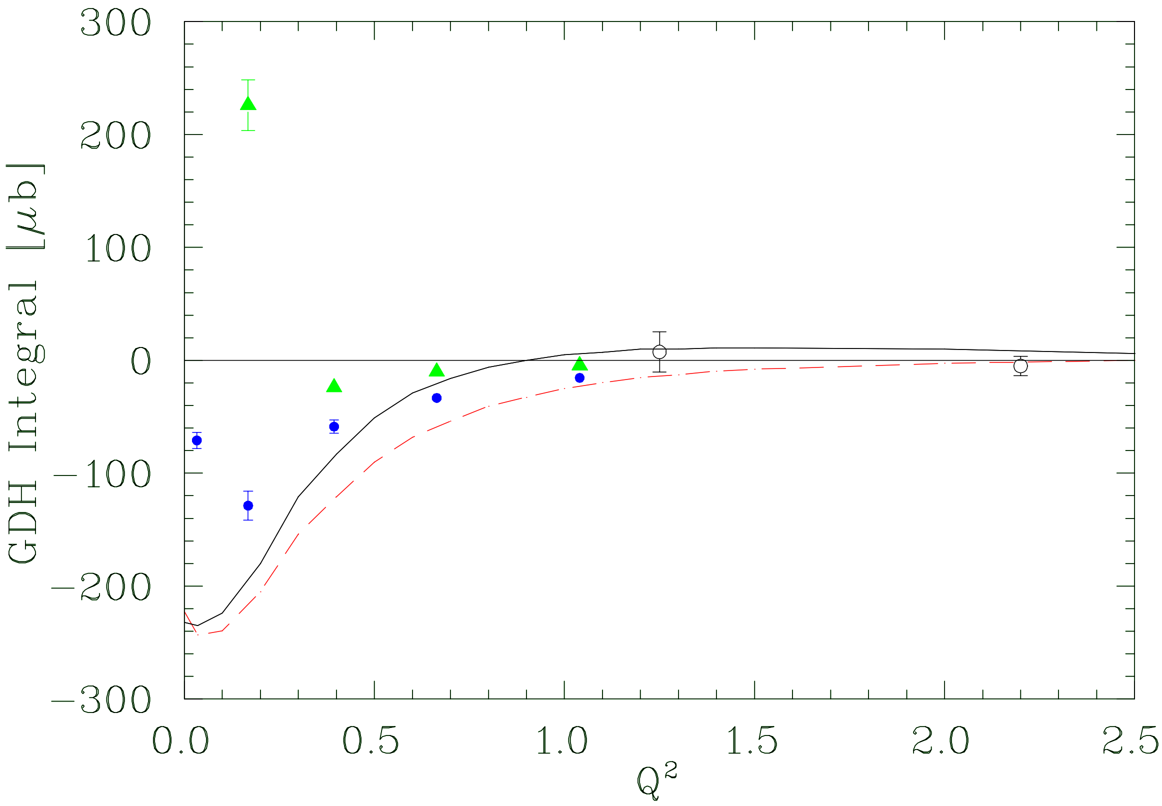

Figure 5.14: The GDH integral. The solid blue circles are results of a neutron extraction from this experiment (Eq. 5.12). The solid green triangles are results of an integration that includes the quasi-elastic peak. A 10% systematic uncertainty is placed on each extracted point of the GDH integral. The statistical uncertainty is negligible. The open black circles are results from Hermes [4] for a neutron. The solid line is the calculation performed by Burkert and Li [1] of the evolution of the GDH integral for a free neutron. The dashed line is the same calculation including only the Δ contribution.

Chapter 6 Conclusion

Jefferson Lab experiment E94-010 marks the first time the polarized ^{3}He cross sections have been measured at low Q^2. The measurements provide information in the quasi-elastic and resonance regions. At this time the analysis is still preliminary, but it does raise some interesting questions concerning the GDH integral for the neutron and ^{3}He. For the neutron, extrapolation of the GDH integral towards $Q^2 = 0$ is far from the real photon point. Uncertainties to be investigated may move the data more in line with predictions, but further measurement in this region is required. For ^{3}He, the GDH integral is expected to have dramatic behavior at very low Q^2 as a result of the data from this experiment. This dramatic behavior would be a direct consequence of the differences between real and virtual photons.

What is needed now is an experiment dedicated toward measuring the polarized ^{3}He cross section in the low to very low Q^2 region. Fortunately, such an experiment is set to take data in the summer of 2002. Jefferson Lab experiment E97-110, *The GDH Sum Rule and the Spin Structure of ^{3}He and the Neutron Using Nearly Real Photons*, will take data on the polarized ^{3}He cross sections at lower Q^2 and higher ν compared to E94-010 (Figure 6.1).

Increasing the kinematic coverage beyond that of E94-010 is made possible by the installation of two septum magnetics. A septum magnetic is a dipole magnet constructed to deflect electrons. The magnet will allow for measurements at more forward angles than currently possible in Hall A. Electrons scattering at an angle of 6° will be possible, whereas presently the minimum angle is 12.5°. This magnet will be added by moving the target upstream and placing them at the previous target location. Implementing this change reduces the angular acceptance from 7.2 msr to 3.7 msr and worsens the momentum resolution from 1.0×10^{-4} to 2.0×10^{-4}, but the

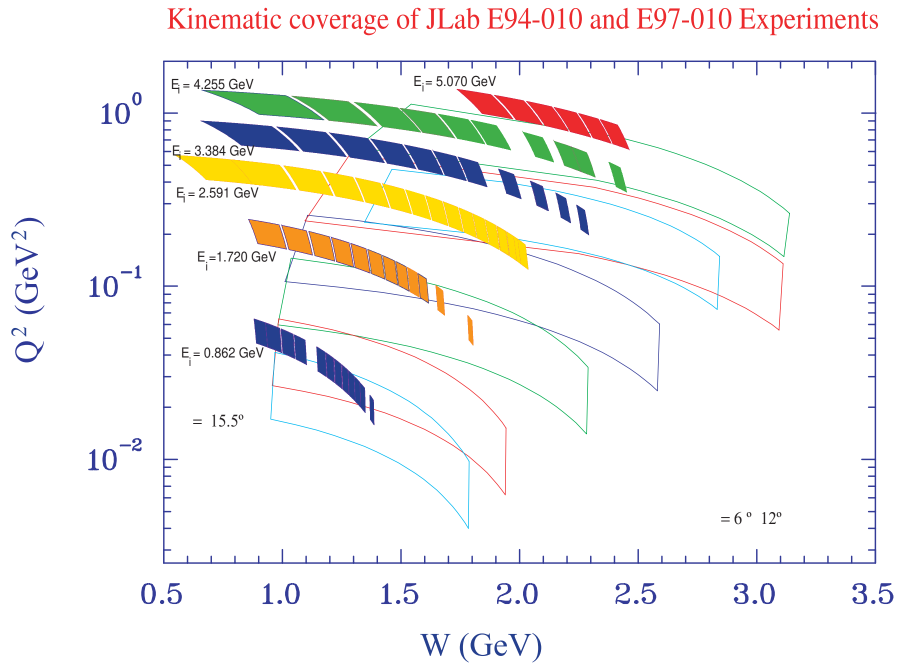

Figure 6.1: Comparison of kinematic coverage for experiments E94-010 and E97-110. The solid boxes represent the measured kinematic of E94-010. The open boxes represent the proposed kinematic coverage of E97-110.

total momentum range should remain unchanged (from 0.4 to 4.0 GeV).

Other than the septum magnetic, experiment E97-110 mirrors E94-010 in a number of ways. It will use six beam energies: 1.6, 2, 3, 4, 5, and 6 GeV. The scattered electrons will cover the ^{3}He quasi-elastic, resonance, and deep inelastic regions. It will use the same polarized ^{3}He target and polarized beam. It will also run for about the same amount of time: 3 months.

With the proposed data, more contributions to the GDH integral will be extracted (Figure 6.2). The goal of the experiment is to extrapolate the GDH integral to Q^2=0 and determine its slope at that point. Chiral perturbation theory predicts a positive

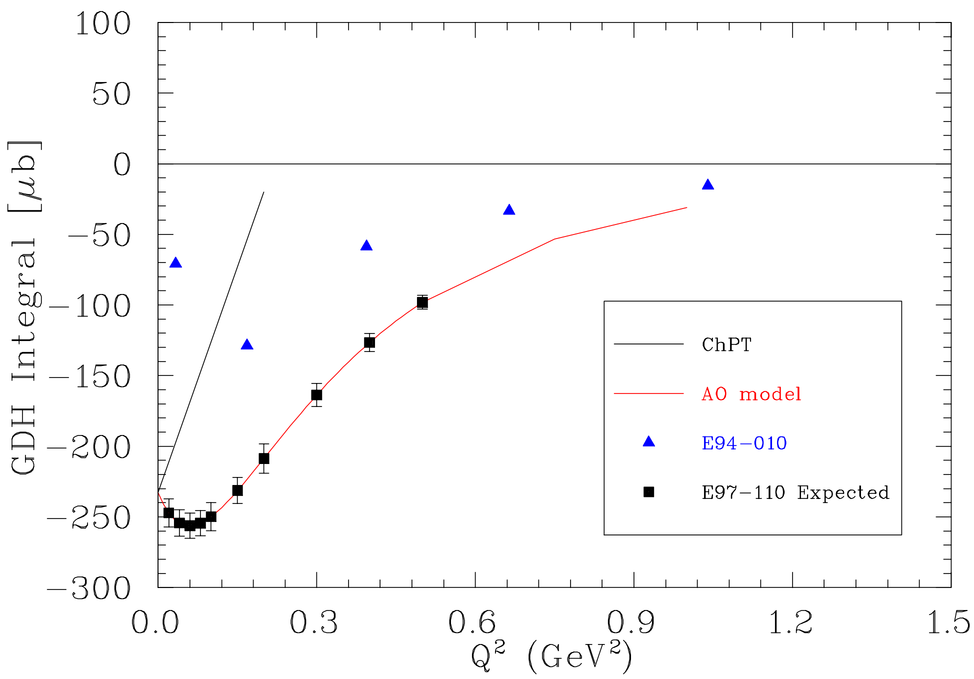

Figure 6.2: Expected precision of the E97-110 experiment for the measurement of the GDH integral. Error bars are systematic and statistical uncertainties added in quadrature.

slope [83], whereas phenomenological models predict a negative slope [1].

Experiment E94-010 and soon E97-110 are just two experiments in a long history of polarized electron scattering experiments. Early experiments sought to understand the spin structure at high Q^2. In this regime nuclear effects are small and the picture of the nucleon is one of quark and gluon interactions. It is described using perturbative QCD. These experiments determined the contribution of the quarks to the total nucleon spin and verified the Bjorken sum rule.

In contrast, this experiment collected data in the transition region between two regimes. One regime is that of the earlier experiments where quark-gluon interactions dominate. The other regime considers ^{3}He as a set of coherent hadrons. The experimental data of Jefferson Lab experiment E94-010 represents a first step towards understanding the transition region using polarized ^{3}He scattering. The hope is that someday a consistent theory across all energies (such as lattice QCD) will be developed.

Bibliography

[1] V. Burkert and Z. Li, Physical Review D **47**, 46 (1993).

[2] C. C. degli Atti and S. Scopetta, Physics Letters B **404**, 223 (1997).

[3] K. Abe *et al.*, Physical Review Letters **79**, 26 (1997).

[4] K. Ackerstaff *et al.*, Physics Letters B **444**, 531 (1998).

[5] J. Ashman *et al.*, Physics Letters B **206**, 364 (1988).

[6] J. Ashman *et al.*, Nuclear Physics B **328**, 1 (1989).

[7] G. P. Ramsey, hep-ph/9702227 (unpublished).

[8] Alguard *et al.*, Physical Review Letters **41**, 70 (1978).

[9] G. Baum *et al.*, Physical Review Letters **51**, 1135 (1983).

[10] B. Adeva *et al.*, Physical Review D **58**, 364 (1998).

[11] P. Anthony *et al.*, Physical Review D **55**, 6620 (1996).

[12] K. Abe *et al.*, Physical Review D **58**, 112003 (1998).

[13] P. Anthony *et al.*, Physics Letters B **463**, 339 (1999).

[14] A. Airapetian *et al.*, Physics Letters B **442**, 484 (1998).

[15] E. Hughes and R. Voss, Annual Review of Nuclear and Particle Science **49**, 303 (1999).

[16] S. Boffi, C. Giusti, and F. Pacati, Physics Reports **226**, 1 (1993).

[17] N. d'Hose, Physics from MAMI and ELSA to ELFE (unpublished).

[18] T. Donnelly and A. Raskin, Annuals of Physics **169**, 247 (1986).

[19] P. Dunn *et al.*, Physical Review C **27**, 71 (1983).

[20] F. Close, *An Introduction to Quarks and Partons* (Academic Press, New York, 1979).

[21] J.L.Friar *et al.*, Physical Review C **42**, 2310 (1990).

[22] V. W. Hughes and J. Kuti, Annual Review of Nuclear and Particle Science **33**, 611 (1983).

[23] U. Stiegler, Physics Reports **277**, 1 (1996).

[24] K. Althoff *et al.*, Z. Phys. **327**, 327 (1979).

[25] V. Burkert, Jefferson Lab publication: PR-93-035 (unpublished).

[26] J. Bjorken, Physical Review **148**, 1467 (1966).

[27] S. Larin, F. Tkackev, and J. Vermaseren, Physical Review Letters **66**, 862 (1991).

[28] S. Gerasimov, Soviet Journal of Nuclear Physics **2**, 430 (1966).

[29] S. Drell and A. Hearn, Physical Review Letters **16**, 908 (1966).

[30] M. Gell-Mann, M. Goldberger, and W. Thirring, Physical Review **95**, 1612 (1954).

[31] G. Arfken, *Mathematical Methods for Physicists* (Academic Press, New York, 1985).

[32] F. Low, Physical Review **96**, 1428 (1954).

[33] M. Gell-Mann and M. Goldberger, Physical Review **96**, 1433 (1954).

[34] D. Drechsel, Progress in Particle and Nuclear Physics **34**, 181 (1995).

[35] M. Anselmino, B. Ioffe, and E. Leader, Soviet Journal of Nuclear Physics **49**, 136 (1989).

[36] X. Ji and J. Osborne, hep-ph/9905410 (unpublished).

[37] R. Alley *et al.*, Nuclear Instruments and Methods in Physics Research A **365**, 1 (1995).

[38] R. Prepost and T. Maruyama, Annual Review of Nuclear and Particle Science **45**, 41 (1995).

[39] A. Glamazdin, Fizika B **8**, 91 (1999).

[40] D. Griffiths, *Introduction to Electrodynamics* (Prentice Hall, New Jersey, 1989).

[41] L. Levchuk, Nuclear Instruments and Methods in Physics Research A **345**, 496 (1994).

[42] K. Unser, IEEE Transactions on Nuclear Science **16**, 934 (1969).

[43] V. Pascal, Nuclear Physics News **9**, 12 (1999).

[44] D. H. Perkins, *Introduction to High Energy Physics* (Addison-Wesley, London, 1982).

[45] K. Fissum *et al.*, MIT-LNS Internal Report #0397 (unpublished).

[46] J. Jackson, *Classical Electrodynamics* (Wiley, New York, 1975).

[47] M. Iodice *et al.*, Nuclear Instruments and Methods in Physics Research A **411**, 223 (1998).

[48] K. Slifer, E94-010 Technical Report #32 (unpublished).

[49] K. R. McCormick, Ph.D. thesis, Old Dominion University, 1999.

[50] M. V. Romalis, Ph.D. thesis, Princeton University, 1997.

[51] W. Happer, Review of Modern Physics **44**, 169 (1972).

[52] A. B.-A. Baranga *et al.*, Physical Review Letters **80**, 2801 (1998).

[53] T. Chupp *et al.*, Physical Review C **36**, 2244 (1987).

[54] W. Happer *et al.*, Physical Review A **29**, 3092 (1984).

[55] S. Applet *et al.*, Physical Review A **58**, 1412 (1998).

[56] M. Wagshul and T. Chupp, Physical Review A **49**, 3854 (1994).

[57] T. Killian, Physical Review **27**, 578 (1926).

[58] S. Appelt *et al.*, Applied Physics Letters **75**, 427 (1999).

[59] K. Moller, *Optics* (University Science Books, California, 1988).

[60] I. Kominis, E95-010 Technical Note #25 (unpublished).

[61] M. Romalis, E. Miron, and G. Cates, Physical Review A **56**, 4569 (1997).

[62] B.Larson *et al.*, Physical Review A **44**, 3108 (1991).

[63] P. of Nuclear Magnetism, *A. Abragam* (Oxford University Press, Oxford, 1994).

[64] H. Goldstein, *Classical Mechanics* (Addison-Wesley, Reading, Massachusetts, 1980).

[65] M. Romalis and G. Cates, Physical Review A **58**, 3004 (1998).

[66] J. Simpson and H. Carr, Physical Review **111**, 1201 (1956).

[67] S. Meiboom, Journal of Chemical Physics **34**, 375 (1961).

[68] G. K. Woodgate, *Elementary Atomic Structure* (Oxford University Press, Oxford, 1989).

[69] J. Kestin *et al.*, Journal of Physical Chemistry (Reference Data) **13**, 229 (1984).

[70] A. Deur, E94-010 Technical Report #33 (unpublished).

[71] E. Offermann and M. Kuss, ESPACE Manual Version 2.7.0 (1998) (unpublished).

[72] K. Slifer, E94-010 Technical Report #31 (unpublished).

[73] A. Deur, E94-010 Technical Report #29 (unpublished).

[74] H. Gao, Ph.D. thesis, Massachusetts Institue of Technology, 1999.

[75] N. Liyanage, Hall A Technical Report (unpublished).

[76] J. LeRose, hallaweb.jlab.org/news/minutes/tranferfuncs.html (unpublished).

[77] L. Mo and Y. Tsai, Review of Modern Physics **41**, 205 (1969).

[78] T. Kuchto and N. Shumeiko, Nuclear Physics 412 (1983).

[79] I. Akushevich and N. Shumeiko, Journal of Physics 513 (1994).

[80] S. Wandzura and F. Wilczek, Physics Letters 195 (1977).

[81] J. Chen, E94-010 spokesperson, private comunitation (unpublished).

[82] R. Pantforder, Ph.D. thesis, Physikalisches Institut der Universitat Bonn, 1998.

[83] G. Cates, J. Chen, and F. Garibaldi, E94-110 proposal (unpublished).